

# Bremsstrahlung Gamma Ray as a Probe of Short-Range Correlations in Nuclei

Junhuai Xu,<sup>1,\*</sup> Qinglin Niu,<sup>2</sup> Yuhao Qin,<sup>1,†</sup> Dawei Si,<sup>1</sup> Yijie Wang,<sup>1</sup> Sheng Xiao,<sup>1</sup> Baiting Tian,<sup>1</sup> Zhi Qin,<sup>1</sup> Haojie Zhang,<sup>1</sup> Boyuan Zhang,<sup>1</sup> Dong Guo,<sup>1</sup> Minxue Fu,<sup>1</sup> Xiaobao Wei,<sup>3</sup> Yibo Hao,<sup>3</sup> Zengxiang Wang,<sup>3</sup> Tianren Zhuo,<sup>3</sup> Chunwang Ma,<sup>3,4</sup> Yuansheng Yang,<sup>5</sup> Xianglun Wei,<sup>5</sup> Herun Yang,<sup>5</sup> Peng Ma,<sup>5</sup> Limin Duan,<sup>5</sup> Fangfang Duan,<sup>5</sup> Kang Wang,<sup>5</sup> Junbing Ma,<sup>5</sup> Shiwei Xu,<sup>5</sup> Zhen Bai,<sup>5</sup> Guo Yang,<sup>5</sup> Yanyun Yang,<sup>5</sup> Mengke Xu,<sup>6</sup> Kaijie Chen,<sup>6</sup> Zirui Hao,<sup>6</sup> Gongtao Fan,<sup>6</sup> Hongwei Wang,<sup>6</sup> Chang Xu,<sup>2,‡</sup> and Zhigang Xiao<sup>1,7,§</sup>

<sup>1</sup>*Department of Physics, Tsinghua University, Beijing 100084, China*

<sup>2</sup>*School of Physics, Nanjing University, Nanjing 210093, China*

<sup>3</sup>*Institute of Particle and Nuclear Physics, Henan Normal University, Xinxiang 453007, China*

<sup>4</sup>*Institute of Nuclear Science and Technology, Henan Academy of Sciences, Zhengzhou, 450015, China*

<sup>5</sup>*Institute of Modern Physics, Chinese Academy of Sciences, Lanzhou 730000, China*

<sup>6</sup>*Shanghai Advanced Research Institute, Chinese Academy of Sciences, Shanghai 201210, China*

<sup>7</sup>*Center of High Energy Physics, Tsinghua University, Beijing 100084, China*

(Dated: April 22, 2025)

The nucleons in nuclei form temporally correlated pairs in close proximity, called short range correlation (SRC), which plays a crucial role in understanding nuclear structure and the fundamental properties of dense nuclear matter. The consequence of SRC on heavy-ion collisions (HICs) has remained unexplored until now. In this paper, we identify neutron-proton bremsstrahlung  $\gamma$ -ray emission from HICs as a new indicator of SRC in nuclei. By observing the hardening of the bremsstrahlung  $\gamma$ -ray spectrum, which results from the increase of high-momentum components above the Fermi surface in nucleon momentum distributions, we precisely determine the SRC fraction in nuclei to be  $(21 \pm 7)\%$  at  $3\sigma$  confidence levels. Our experiment identifies the first direct and accurate signature of SRC in low-energy HICs, providing a new method to study the parton momentum distribution of nucleons in nuclei.

*Introduction* – Nucleonic matter is one of the strong-interacting forms of matter across vastly different scales from atomic nuclei to neutron stars in the Universe. Understanding how the nucleons interact is of fundamental importance to reproduce the static and dynamical properties of nucleonic matter [1]. While protons and neutrons are made up of quarks, quark-level interactions are neglected in most nuclear models based on mean-field approach, like nuclear shell model [2]. In the conventional picture, the momenta of nucleons are constrained below the Fermi momentum and the partonic structure functions of bound and free nucleons are identical. However, the deep inelastic scattering (DIS) experiments conducted by the European Muon Collaboration (EMC) observed that the nucleon structure function in deuterons differs from that in heavy nuclei. This phenomenon, known as the EMC effect [3], indicates that the internal quark distribution plays a role in nuclear structure and the nucleon momentum distribution deviated from shell model predictions [4–9].

To clarify the origin of the deviation of nucleon momentum from the Fermi distribution, scientists identified short-range correlation (SRC) between nucleons [4, 10], which is a temporal fluctuation effect beyond mean-field. More evidences demonstrate that the EMC effect and the presence of SRC are closely connected at quark level and

the abundance of SRC pairs influences the EMC effect in different nuclei [11–13], indicating that by studying SRC one can potentially learn the parton distribution functions (PDF) of nucleons in nuclei.

The majority of our present understanding to SRC in atomic nuclei comes from the electron-nucleus scattering [10, 14–17] and proton-nucleus knockout [18–20] experiment. A recent global analysis based on QCD factorization scheme extracts the universal effective distribution of partons inside SRC pairs and the mean-field fraction using a variety of high-energy data [21]. Existing studies found that the SRC can be predominantly characterized by neutron-proton ( $np$ ) pairing in the isosinglet ( $T=0$ ) channel at short distance, which favors  $ud$  diquark isosinglet and spin singlet pairing at quark level [22]. SRC also enhances the high-momentum components of the nucleon momentum distribution above the Fermi surface in nuclei, forming a “high-momentum tail” (HMT) that is absent in the mean-field picture [10, 17]. The presence of HMT have strong impact on the properties of dense nucleonic matter, particularly the density dependence of the nuclear symmetry energy [23–25].

Among various experimental approaches, heavy-ion collisions (HICs) offer a unique opportunity to create bulk dense nucleonic matter in a terrestrial laboratory. Therefore, searching for signatures of SRC in HICs is of significant importance, as it not only bridges SRC and dense nucleonic matter, but also helps determine the SRC fraction, thereby validating the accuracy and reliability of previous measurements. When two heavy nuclei collide, two-body  $np$  collisions produce bremsstrahlung  $\gamma$ -rays [26–28]. Due to the influence of the HMT, the

\* xjh22@mails.tsinghua.edu.cn

† qinyh18@tsinghua.org.cn

‡ cxu@nju.edu.cn

§ xiaozg@tsinghua.edu.cn

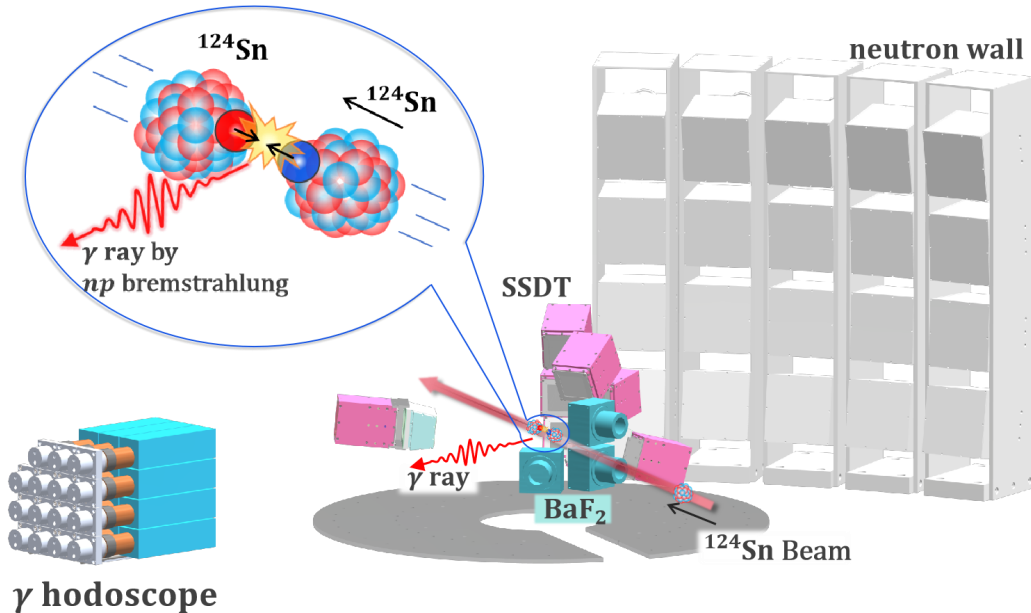


FIG. 1: Illustration of the CSHINE detector setup with a schematic view of an  $^{124}\text{Sn}+^{124}\text{Sn}$  event marked by a  $np$  collision, producing an energetic bremsstrahlung  $\gamma$  photon which is detected by the CsI(Tl) hodoscope. Four scintillators are mounted surrounding the hodoscope (not shown) to veto the cosmic muons as well as the  $\gamma$  events with energy leakage to outside.

average nucleon kinetic energies of both projectile and target increase significantly, causing the emitted  $\gamma$ -ray spectrum to harden, particularly at high energies [29]. Advantageously, these high-energy  $\gamma$ -rays are largely unaffected by the nuclear medium, making them an effective and novel probe for detecting SRC effects [29–31].

Theoretical calculations using the Isospin-dependent Boltzmann-Uehling-Uhlenbeck (IBUU) transport model [32], adopting Momentum-Dependent Interaction (MDI) [33], predict the bremsstrahlung  $\gamma$ -ray spectra produced in HICs by varying the HMT ratio ( $R_{\text{HMT}}$ ) [29]. This ratio represents the fraction of high-momentum components above the Fermi surface in the nucleon momentum distributions in nuclei [29]. By comparing the model predictions with experimental  $\gamma$ -ray spectra, the HMT ratio can be constrained, offering potentially an innovative method to probe the parton momentum distributions in correlated  $np$  pairs in nuclei.

*Experiments and Data Analysis* – The Compact Spectrometer for Heavy Ion Experiment (CSHINE), located at the end of Radioactive Ion Beam Line 1 (RIBLL1) at the Heavy Ion Research Facility in Lanzhou (HIRFL), is designed to study HICs at Fermi energies [34, 35] (see

Fig. 1). Charged particles produced in the final state are detected using silicon-strip telescopes (SSDTs) [36]. Neutrons are identified by an array of 20 plastic scintillators, while  $\text{BaF}_2$   $\gamma$ -detectors surrounding the target provide starting time ( $T_0$ ) information [37]. To measure energetic bremsstrahlung  $\gamma$ -rays from reactions at the target, a  $4 \times 4$  CsI(Tl)-based hodoscope has been installed [38], allowing the detection of photons with energies up to 100 MeV. Each unit has dimensions of  $7 \times 7 \times 25 \text{ cm}^3$ . The trigger system of CSHINE is implemented using field-programmable gate array (FPGA) technology [39].

In the experiment involving  $^{86}\text{Kr}+^{124}\text{Sn}$  reactions at a beam energy of 25 MeV per nucleon, the bremsstrahlung  $\gamma$ -ray spectrum was successfully measured using CSHINE, revealing a high-momentum nucleon fraction of  $R_{\text{HMT}} \sim 15\%$  in the  $\gamma$  energy range between 35 and 80 MeV. This was achieved through comparison with predictions from the IBUU-MDI transport model [40]. To mitigate the effects of detector filtering, a deblurring algorithm was developed to reconstruct the original  $\gamma$  spectrum, which further indicated the presence of high-momentum tails (HMT) with a ratio of  $R_{\text{HMT}} \sim 25\%$  [41]. However, the limited energy range

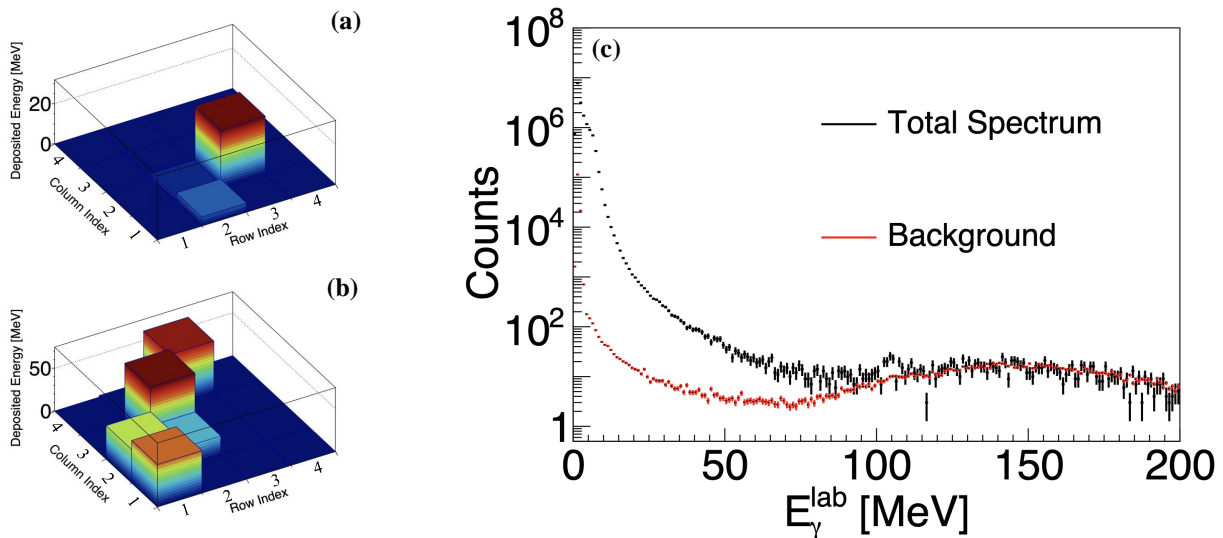


FIG. 2: (Color Online) (a) The event display of a high energy  $\gamma$  from the reaction. (b) The event display of a cosmic  $\mu$  penetration event through the  $\gamma$ -hodoscope. (c) The experimental  $\gamma$  energy spectrum in laboratory reference measured in reactions with beam on (black), in comparison to the background spectrum recorded with beam off (red). The background spectrum is scaled by a normalization factor determined in the energy range above 110 MeV. Both spectra are calibrated using the same calibration datasets.

and low statistics restrict the accuracy of the result.

To overcome these limitations, a new experiment was conducted using  $^{124}\text{Sn}+^{124}\text{Sn}$  reactions at 25 MeV per nucleon beam energy [37]. A plastic scintillator array was installed around the CsI(Tl) hodoscope to veto the cosmic ray background as well as the  $\gamma$  events with energy leakage to the outside. Additionally, the energy range of the individual scintillators was extended to reach the maximum detectable energy of 100 MeV for bremsstrahlung  $\gamma$ -rays. These advancements enabled a high-confidence determination of the  $R_{\text{HMT}}$  associated with SRC, leveraging high-energy  $\gamma$ -ray emissions from HICs.

After calibrating the CsI(Tl) hodoscopes, the energy deposit in the hodoscope is reconstructed on an event-by-event basis. The reconstruction algorithm identifies clustered CsI(Tl) hits in each event and classifies them as either a  $\gamma$ -ray event or a penetrating cosmic muon. Figures 2(a) and (b) illustrate a typical  $\gamma$ -ray event and a penetrating cosmic ray event detected by the CsI(Tl) hodoscopes, respectively. It is clearly observed that the penetrating cosmic muon results in a large spatial extension of the CsI(Tl) hits and likely leaves hits in the surrounding scintillators, demonstrating a significantly different pattern compared to the  $\gamma$ -ray event. To subtract the background, which mainly includes cosmic muons and low-energy residual  $\gamma$ -rays, the background spectrum is measured when the beam is off. Figure 2(c) shows the total  $\gamma$  spectrum (black histogram) and the background spectrum (red), which is scaled to match the total spectrum based on the counts above 110 MeV. The pure  $\gamma$  spectrum is then obtained by subtracting the scaled

background spectrum from the total spectrum.

Since the detected  $\gamma$ -ray spectrum is influenced by the detector efficiency, theoretical curves must be processed through the detector filter before comparing them to experimental data. Using Geant4 simulations, the CsI array's response to  $\gamma$ -rays of varying energies was modeled to generate a detector filter matrix in the laboratory frame [38]. Each element of the matrix represents the probability,  $P_i(E_j)$ , of a photon with energy  $E_j$  producing a response  $E_i$  in the detector. For spectra limited to energies  $E \leq 100$  MeV, the matrix is a  $100 \times 100$  array, with energy ranging from 1 to 100 MeV in 1 MeV step. To enable direct comparison with experimental data, the theoretical curves are transformed into the laboratory frame, processed using the detector filter matrix, and then converted back to the center-of-mass (c.m.) frame. During the conversion of the spectrum between the laboratory and the c.m. frame, the photon Doppler effect is taken into account, which causes a slight softening of the energy spectrum.

The statistical uncertainties in the  $\gamma$  spectrum follow a Poisson distribution. The Poisson error for each bin is calculated based on the counts in the original spectrum and is propagated through all subsequent operations performed on the spectrum. The most significant systematic uncertainty arises from the calibration process. Since the maximum energy of the radioactive source used for calibration is below 3 MeV, additional high-energy  $\gamma$  beam tests were conducted to characterize the detector's response at higher  $\gamma$  energies [42]. These tests resulted in two typical detector response correction functions.

To evaluate the systematic uncertainties, nine distinct

$\gamma$  spectra were generated using the two detector response correction functions in conjunction with linear calibration, along with three calibration datasets from radioactive sources that account for the time shift of the detector and electronics. Of these, the spectrum derived from the calibration datasets with the highest statistics and the initially two-range linear calibration method [42] was designated as the central spectrum. The remaining spectra were then used to estimate the systematic uncertainties by calculating the standard deviation of their values in each energy bin.

*Results and Discussions* – Fig. 3 illustrates the rebinned experimental  $\gamma$  spectrum in the c.m. frame. The black dots represent the central spectrum, with statistical uncertainties indicated by error bars, and the gray shaded regions denote the systematic uncertainties at each energy point. Several key theoretical curves, processed with the detector filter, are presented for comparison. Unlike in our previous experiment [40, 41], in this experiment, the  $\gamma$  detector array was operated in active triggering mode, preventing the determination of the number of  $np$  collisions in heavy-ion reactions as a normalization factor for the  $\gamma$  spectrum. Consequently, the comparison between experimental data and theoretical curves predicted by the IBUU model focused on spectral shape similarities rather than absolute normalization. To align the range of the theoretical curves with the experimental spectrum, the theoretical values were uniformly scaled by a factor of  $2.5 \times 10^9$ , which had no impact on determining the  $R_{\text{HMT}}$ , as it did not affect the comparison of shape differences between the experimental and model-predicted spectra.

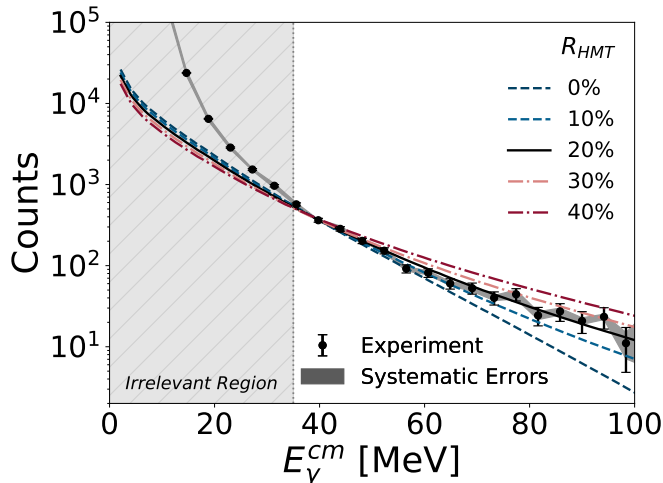


FIG. 3: (Color Online) Comparison of the rebinned experimental  $\gamma$  spectrum (black dots) with statistical uncertainties (error bars) and systematic uncertainties (gray shaded areas) in the c.m. frame. Several key theoretical curves, processed with the detector filter, are overlaid for comparison.

The comparison between the IBUU model and the ex-

perimental data was performed using the maximum likelihood analysis method. The likelihood function was defined as [40]

$$\ln L'(R_{\text{HMT}}) = \sum_i^{\text{range}} n_i \ln p_i(R_{\text{HMT}}). \quad (1)$$

where  $i$  denotes the sum of experimental points within a certain statistical analysis interval, and  $n_i$  represents the counts of the  $i^{\text{th}}$  experimental data point. The quantity  $p_i$  represents the probability that the theoretical model predictions fall into the corresponding histogram bin of the experimental data under the specified statistical analysis interval for a given  $R_{\text{HMT}}$ . Energies below 30 MeV are primarily influenced by collective resonance and statistical emissions. Therefore, we selected an energy range of  $35 < E_\gamma^{\text{cm}} < 100$  MeV as the central analysis interval and calculated the likelihood function between the experimental  $\gamma$  spectrum at each point within this range and various IBUU theoretical curves.

The results are presented as blue dots with error bars in Fig. 4(a), where the central values are derived from the central  $\gamma$  spectrum. To standardize the likelihood function values obtained from different  $\gamma$  spectra, the likelihood corresponding to the theoretical curve with  $R_{\text{HMT}} = 0\%$  was selected as the reference point ( $\ln L'(R_{\text{HMT}} = 0\%) = 0$ ). The relative likelihood values,  $\Delta \ln L'(R_{\text{HMT}})$ , for all other points were calculated relative to this baseline. The error bars at each  $R_{\text{HMT}}$  represent the standard deviations of the relative likelihood values obtained from the other  $\gamma$  spectra with the corresponding  $R_{\text{HMT}}$ .

The likelihood function reaches its maximum near  $R_{\text{HMT}} = 20\%$  and follows an approximately quadratic distribution. This trend was fitted with a quadratic function, depicted as the blue dashed curve in the figure, which yielded a maximum value at  $R_{\text{HMT}} \approx 21\%$ . Based on the likelihood function distribution, the confidence intervals for the  $R_{\text{HMT}}$  are indicated by the black dashed lines in the figure. Therefore, based on the experimentally measured  $\gamma$  spectrum, the  $R_{\text{HMT}}$  value can be determined at a  $3\sigma$  confidence level, yielding  $R_{\text{HMT}} = (21 \pm 7)\%$ .

To compare the experimental result with theoretical predictions without detector filtering, the original  $\gamma$  spectrum was reconstructed from the measured spectrum using the Richardson-Lucy (RL) algorithm [41]. The best value of  $R_{\text{HMT}}$  was determined by minimizing the  $\chi^2(R_{\text{HMT}})$ , which compares the reconstructed spectrum to the theoretical predictions. The  $\chi^2(R_{\text{HMT}})$  is given by the following expression [41]

$$\chi^2(R_{\text{HMT}}) = \sum_i \frac{1}{\sigma_i^2} (n_i^{\text{exp}} - n_i^{R_{\text{HMT}}})^2, \quad (2)$$

where  $n_i^{\text{exp}}$  represents the experimental data counts in the  $i^{\text{th}}$  energy bin,  $n_i^{R_{\text{HMT}}}$  is the theoretical counts at a

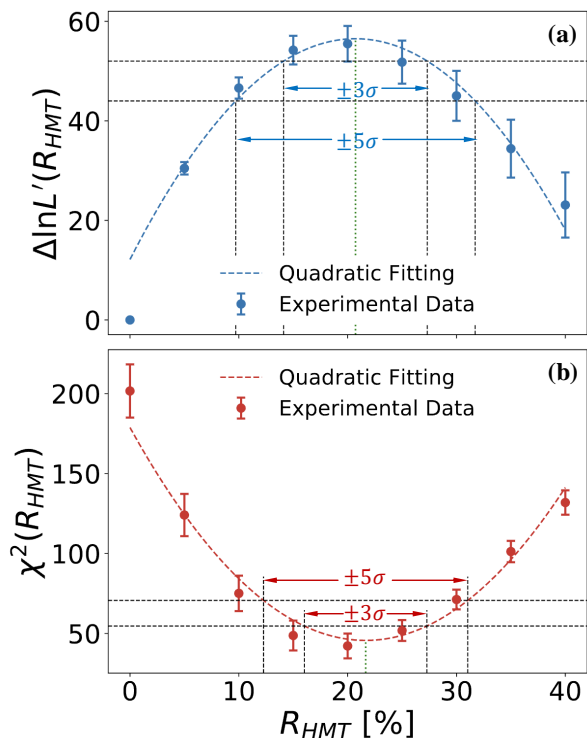


FIG. 4: (Color Online) Fitting results for  $R_{\text{HMT}}$  using two methods. (a) Forward analysis: the theoretical spectra were filtered by detector response and compared with the experimental spectra via the likelihood function. (b) Inverse analysis: experimental spectrum was reconstructed to the original  $\gamma$ -ray spectra by RL algorithm and directly compared to theoretical spectra via the  $\chi^2$  test. Solid dots represent results from the central  $\gamma$  spectrum, with error bars representing the standard deviation of likelihood function ( $\chi^2$ ) values obtained from other  $\gamma$  spectra, generated using different calibration datasets and detector response models. Blue and red dashed curves are quadratic fits, with the vertex indicating the optimal  $R_{\text{HMT}}$ . Black dashed lines mark the  $\pm 3\sigma$  and  $\pm 5\sigma$  confidence levels.

given  $R_{\text{HMT}}$  in the same bin, and  $\sigma_i$  is the uncertainty in the reconstructed spectrum for the  $i^{\text{th}}$  energy bin.

In the energy range of interest, the  $\chi^2(R_{\text{HMT}})$  distribution is shown as red dots with error bars in Fig. 4(b). A quadratic fit to this distribution, represented by the red dashed line, reveals that the minimum occurs at  $R_{\text{HMT}} \approx 22\%$ . The confidence intervals for  $R_{\text{HMT}}$  were determined based on the  $\chi^2$  distribution, as indicated by the black dashed lines in the figure. Therefore, the optimal value of  $R_{\text{HMT}}$  determined from the reconstructed spectrum at the  $3\sigma$  confidence level is  $R_{\text{HMT}} = (22 \pm 6)\%$ . This result is consistent with the forward analysis, within the error margin.

Combining both the forward and inverse analysis re-

sults, it is concluded that the fraction of HMT components in the nucleon momentum distribution at the  $3\sigma$  confidence level is  $R_{\text{HMT}} = (21 \pm 7)\%$ . The look-else-effect, namely the variation caused by changing the low limit of the energy range of interest, is well covered by the quoted uncertainty.

Last but not least, the result has important implication to the studies of binary neutron star merging (BNSM), which is an astrophysics analog of HIC. Bremsstrahlung  $\gamma$ -ray emission in the range of tens MeV or higher from HICs can serve as a signature of accelerated nuclei interacting with the surrounding environment during the violent process of BNSM. Hydrodynamic simulations indicate that nuclear matter at the collision interface of the BNSM event is heated to tens of MeV [43], where intense nucleus-nucleus collisions with high energy  $\gamma$  ray emission are expected. In addition, a recent study predicts that ultra-high-energy cosmic rays may originate from BNSM [44], and similarly high energy  $\gamma$  rays are emitted when the accelerating nuclei collide with the surrounding matter. However, the negative reports regarding high-energy  $\gamma$ -rays in follow-up observations of GW170817 [45] contradict with the speculations and highlight the need for more detailed quantitative modeling of BNSM dynamics.

*Summary* – To summarize, the precise measurement of the  $np$  bremsstrahlung  $\gamma$  rays in  $^{124}\text{Sn} + ^{124}\text{Sn}$  at 25 MeV/u not only resolves the puzzle that emerged in the 1980s regarding the origin of high-energy  $\gamma$ -rays in HICs [46], but also identifies a new indicator of SRC, which is a significant phenomenon relevant to nuclear structure as well as to the properties of dense nucleonic matter.

We leverage the advantage of HICs, where the bremsstrahlung  $\gamma$ -ray energy spectrum is hardened due to the HMT of nucleons resulting from SRC. By comparing the experimental  $\gamma$ -ray spectrum with theoretical predictions from the IBUU-MDI transport model, we have precisely determined the ratio of the high-momentum component of the  $np$  momentum distribution,  $R_{\text{HMT}} = (21 \pm 7)\%$  at a  $3\sigma$  confidence level. Both forward and inverse methods yielded consistent results within the uncertainty range, confirming the robustness and reliability of our findings. IBUU-MDI simulations show that bremsstrahlung  $\gamma$ -ray production becomes increasingly sensitive to  $R_{\text{HMT}}$  induced by SRCs in the colliding nuclei, particularly at the high-energy end of the  $\gamma$ -ray spectrum. This underscores the need for further systematic experimental studies of higher-energy  $\gamma$  rays in HICs.

*Acknowledgements.* This work is supported by the Ministry of Science and Technology under Grant No. 2022YFE0103400, by the National Natural Science Foundation of China under Grant Nos. 12335008, 12205160, 12275129, by the Center for High Performance Computing and Initiative Scientific Research Program in Tsinghua University and by the Heavy Ion Research Facility in Lanzhou (HIRFL). The authors acknowledge the HIRFL machine team for providing the excellent beam condition.

- 
- [1] M. Oertel, M. Hempel, T. Klähn, and S. Typel, Equations of state for supernovae and compact stars, *Rev. Mod. Phys.* **89**, 015007 (2017).
- [2] E. Caurier, G. Martinez-Pinedo, F. Nowacki, A. Poves, and A. P. Zuker, The Shell Model as Unified View of Nuclear Structure, *Rev. Mod. Phys.* **77**, 427 (2005), [arXiv:nucl-th/0402046](#).
- [3] J. J. Aubert et al. (European Muon), The ratio of the nucleon structure functions  $F_2^n$  for iron and deuterium, *Phys. Lett. B* **123**, 275 (1983).
- [4] O. Hen, G. A. Miller, E. Piasezky, and L. B. Weinstein, Nucleon-Nucleon Correlations, Short-lived Excitations, and the Quarks Within, *Rev. Mod. Phys.* **89**, 045002 (2017), [arXiv:1611.09748 \[nucl-ex\]](#).
- [5] P. R. Norton, The EMC effect, *Rept. Prog. Phys.* **66**, 1253 (2003).
- [6] D. F. Geesaman, K. Saito, and A. W. Thomas, The nuclear EMC effect, *Ann. Rev. Nucl. Part. Sci.* **45**, 337 (1995).
- [7] S. Malace, D. Gaskell, D. W. Higinbotham, and I. Cloet, The Challenge of the EMC Effect: existing data and future directions, *Int. J. Mod. Phys. E* **23**, 1430013 (2014), [arXiv:1405.1270 \[nucl-ex\]](#).
- [8] J. J. Kelly, Nucleon knockout by intermediate-energy electrons, *Adv. Nucl. Phys.* **23**, 75 (1996).
- [9] W. H. Dickhoff and C. Barbieri, Selfconsistent Green's function method for nuclei and nuclear matter, *Prog. Part. Nucl. Phys.* **52**, 377 (2004), [arXiv:nucl-th/0402034](#).
- [10] O. Hen et al., Momentum sharing in imbalanced Fermi systems, *Science* **346**, 614 (2014), [arXiv:1412.0138 \[nucl-ex\]](#).
- [11] L. B. Weinstein, E. Piasezky, D. W. Higinbotham, J. Gomez, O. Hen, and R. Shneor, Short Range Correlations and the EMC Effect, *Phys. Rev. Lett.* **106**, 052301 (2011), [arXiv:1009.5666 \[hep-ph\]](#).
- [12] O. Hen, E. Piasezky, and L. B. Weinstein, New data strengthen the connection between Short Range Correlations and the EMC effect, *Phys. Rev. C* **85**, 047301 (2012), [arXiv:1202.3452 \[nucl-ex\]](#).
- [13] B. Schmookler et al. (CLAS), Modified structure of protons and neutrons in correlated pairs, *Nature* **566**, 354 (2019), [arXiv:2004.12065 \[nucl-ex\]](#).
- [14] R. Shneor et al. (Jefferson Lab Hall A), Investigation of proton-proton short-range correlations via the C-12( $e, e'$ pp) reaction, *Phys. Rev. Lett.* **99**, 072501 (2007), [arXiv:nucl-ex/0703023](#).
- [15] R. Subedi et al., Probing Cold Dense Nuclear Matter, *Science* **320**, 1476 (2008), [arXiv:0908.1514 \[nucl-ex\]](#).
- [16] I. Korover et al. (Lab Hall A), Probing the Repulsive Core of the Nucleon-Nucleon Interaction via the  $^4\text{He}(e, e'pN)$  Triple-Coincidence Reaction, *Phys. Rev. Lett.* **113**, 022501 (2014), [arXiv:1401.6138 \[nucl-ex\]](#).
- [17] M. Duer et al. (CLAS), Probing high-momentum protons and neutrons in neutron-rich nuclei, *Nature* **560**, 617 (2018).
- [18] A. Tang et al., n-p short range correlations from (p,2p + n) measurements, *Phys. Rev. Lett.* **90**, 042301 (2003), [arXiv:nucl-ex/0206003](#).
- [19] E. Piasezky, M. Sargsian, L. Frankfurt, M. Strikman, and J. W. Watson, Evidence for the strong dominance of proton-neutron correlations in nuclei, *Phys. Rev. Lett.* **97**, 162504 (2006), [arXiv:nucl-th/0604012](#).
- [20] M. Patsyuk et al., Unperturbed inverse kinematics nucleon knockout measurements with a 48 GeV/c carbon beam, *Nature Phys.* **17**, 693 (2021), [arXiv:2102.02626 \[nucl-ex\]](#).
- [21] A. W. Denniston, T. Ježo, A. Kusina, N. Derakhshanian, P. Duwentäster, O. Hen, C. Keppel, M. Klasen, K. Kovařík, J. G. Morfín, K. F. Muzakka, F. I. Olness, E. Piasezky, P. Risse, R. Ruiz, I. Schienbein, and J. Y. Yu., Modification of quark-gluon distributions in nuclei by correlated nucleon pairs, *Phys. Rev. Lett.* **133**, 152502 (2024).
- [22] J. Rittenhouse West, Diquark induced short-range nucleon-nucleon correlations & the emc effect, *Nuclear Physics A* **1029**, 122563 (2023).
- [23] C. Xu and B.-A. Li, Understanding the major uncertainties in the nuclear symmetry energy at suprasaturation densities, *Phys. Rev. C* **81**, 064612 (2010).
- [24] O. Hen, B.-A. Li, W.-J. Guo, L. B. Weinstein, and E. Piasezky, Symmetry energy of nucleonic matter with tensor correlations, *Phys. Rev. C* **91**, 025803 (2015).
- [25] B.-J. Cai and B.-A. Li, Symmetry energy of cold nucleonic matter within a relativistic mean field model encapsulating effects of high-momentum nucleons induced by short-range correlations, *Phys. Rev. C* **93**, 014619 (2016).
- [26] W. Bauer, G. F. Bertsch, W. Cassing, and U. Mosel, Energetic photons from intermediate energy proton- and heavy-ion-induced reactions, *Phys. Rev. C* **34**, 2127 (1986).
- [27] G. Martinez et al., Photon production in heavy ion collisions close to the pion threshold, *Phys. Lett. B* **461**, 28 (1999), [arXiv:nucl-ex/9910006](#).
- [28] N. Gan, K.-T. Brinkmann, A. Caraley, B. Fineman, W. Kernan, R. McGrath, and P. Danielewicz, Neutron-proton bremsstrahlung from low-energy heavy-ion reactions, *Physical Review C* **49**, 298 (1994).
- [29] H. Xue, C. Xu, G.-C. Yong, and Z. Ren, Neutron-proton bremsstrahlung as a possible probe of high-momentum component in nucleon momentum distribution, *Phys. Lett. B* **755**, 486 (2016).
- [30] W.-M. Guo, B.-A. Li, and G.-C. Yong, Imprints of high-momentum nucleons in nuclei on hard photons from heavy-ion collisions near the Fermi energy, *Phys. Rev. C* **104**, 034603 (2021), [arXiv:2106.08242 \[nucl-th\]](#).
- [31] C. Xu, A. Li, and B.-A. Li, Delineating effects of tensor force on the density dependence of nuclear symmetry energy, *J. Phys. Conf. Ser.* **420**, 012090 (2013), [arXiv:1207.1639 \[nucl-th\]](#).
- [32] G. Bertsch and S. Das Gupta, A guide to microscopic models for intermediate energy heavy ion collisions, *Physics Reports* **160**, 189 (1988).
- [33] C. B. Das, S. Das Gupta, C. Gale, and B.-A. Li, Momentum dependence of symmetry potential in asymmetric nuclear matter for transport model calculations, *Phys. Rev. C* **67**, 034611 (2003).
- [34] F. Guan et al., A Compact Spectrometer for Heavy Ion Experiments in the Fermi energy regime, *Nucl. Instrum. Meth. A* **1011**, 165592 (2021).
- [35] Y.-J. Wang et al., CSHINE for studies of HBT correlation in Heavy Ion Reactions, *Nucl. Sci. Tech.* **32**, 4 (2021), [arXiv:2101.07352 \[physics.ins-det\]](#).

- [36] F. Guan *et al.*, Track recognition for the  $\Delta E$ – $E$  telescopes with silicon strip detectors, *Nucl. Instrum. Meth. A* **1029**, 166461 (2022), [arXiv:2110.08261 \[physics.ins-det\]](#).
- [37] D. Si *et al.*, The neutron array of the compact spectrometer for heavy ion experiments in Fermi energy region, *Nucl. Instrum. Meth. A* **1070**, 170055 (2025), [arXiv:2406.18605 \[physics.ins-det\]](#).
- [38] Y. Qin *et al.*, A CsI(Tl) hodoscope on CSHINE for Bremsstrahlung  $\gamma$ -rays in heavy ion reactions, *Nucl. Instrum. Meth. A* **1053**, 168330 (2023), [arXiv:2212.13498 \[physics.ins-det\]](#).
- [39] D. Guo *et al.*, An FPGA-based trigger system for CSHINE, *Nucl. Sci. Tech.* **33**, 162 (2022), [arXiv:2206.15382 \[physics.ins-det\]](#).
- [40] Y. Qin *et al.*, Probing high-momentum component in nucleon momentum distribution by neutron-proton bremsstrahlung  $\gamma$ -rays in heavy ion reactions, *Phys. Lett. B* **850**, 138514 (2024), [arXiv:2307.10717 \[nucl-ex\]](#).
- [41] J. Xu, Y. Qin, Z. Qin, D. Si, B. Zhang, Y. Wang, Q. Niu, C. Xu, and Z. Xiao, Reconstruction of Bremsstrahlung  $\gamma$ -rays spectrum in heavy ion reactions with Richardson-Lucy algorithm, *Phys. Lett. B* **857**, 139009 (2024), [arXiv:2405.06711 \[nucl-th\]](#).
- [42] J. Xu, D. Si, Y. Qin, M. Xu, K. Chen, Z. Hao, G. Fan, H. Wang, and Z. Xiao, Linear Response of CsI(Tl) Crystal to Energetic Photons below 20 MeV, arXiv preprint [arXiv:2503.10098](#) (2025), [arXiv:2503.10098 \[physics.ins-det\]](#).
- [43] E. R. Most, A. Motornenko, J. Steinheimer, V. Dexheimer, M. Hanauske, L. Rezzolla, and H. Stoecker, Probing neutron-star matter in the lab: Similarities and differences between binary mergers and heavy-ion collisions, *Phys. Rev. D* **107**, 043034 (2023).
- [44] G. R. Farrar, Binary neutron star mergers as the source of the highest energy cosmic rays, *Phys. Rev. Lett.* **134**, 081003 (2025).
- [45] B. P. Abbott *et al.*, Multi-messenger observations of a binary neutron star merger\*, *The Astrophysical Journal Letters* **848**, L12 (2017).
- [46] M. Njock, M. Maurel, E. Monnard, H. Nifenecker, J. Pinston, F. Schussler, and D. Barneoud, High energy gamma-ray production in heavy-ion reactions, *Physics Letters B* **175**, 125 (1986).